PCCP

Physical Chemistry Chemical Physics

www.rsc.org/pccp

Volume 15 | Number 15 | 21 April 2013 | Pages 5245–5722

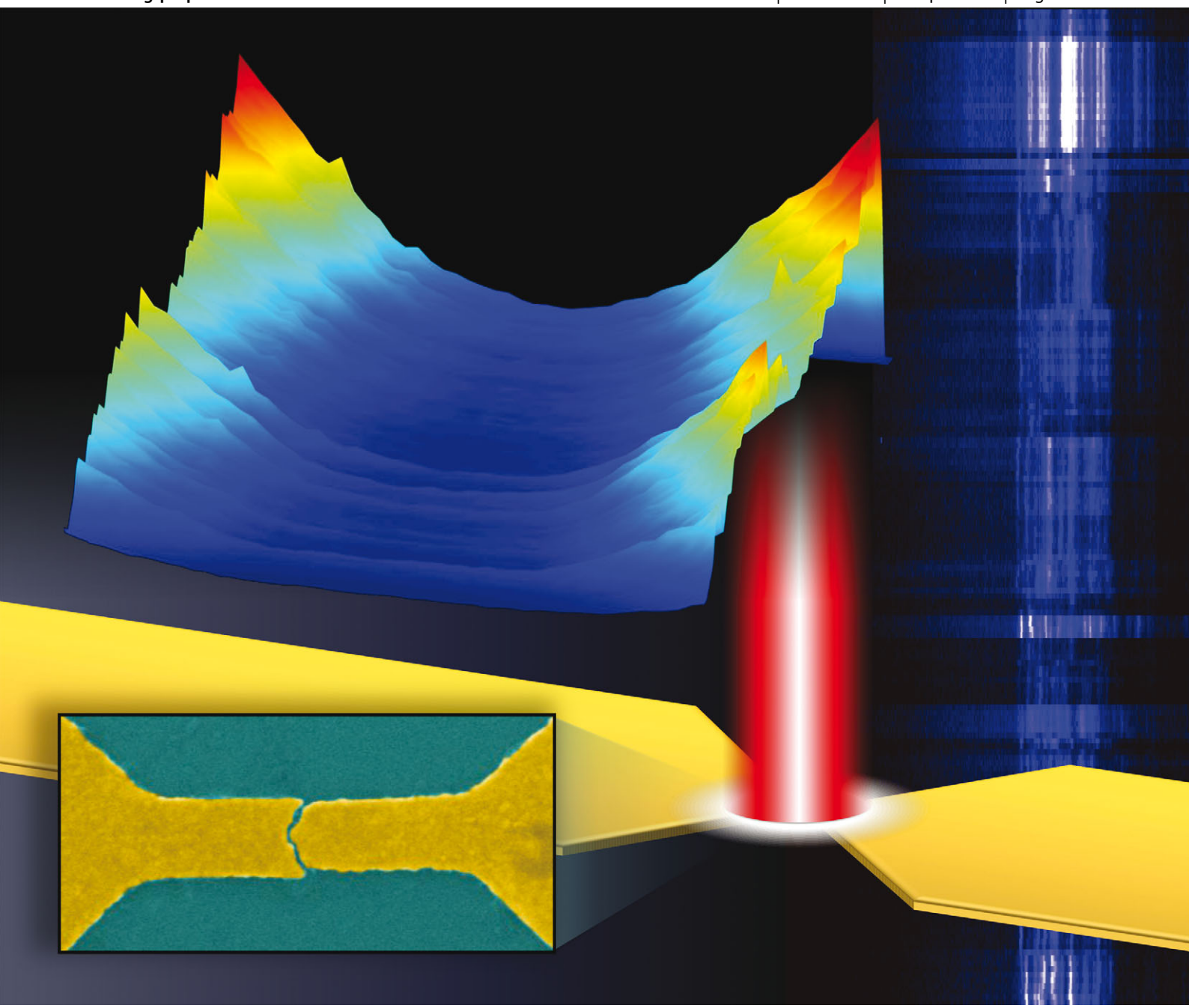

ISSN 1463-9076

PERSPECTIVE

Natelson *et al.*

Nanogap structures: combining enhanced Raman spectroscopy and electronic transport

1463-9076(2013)15:15;1-Q

PCCP

RSC Publishing

PERSPECTIVE

View Article Online
View Journal | View Issue

Nanogap structures: combining enhanced Raman spectroscopy and electronic transport

Cite this: *Phys. Chem. Chem. Phys.*, 2013, **15**, 5262

Douglas Natelson,*[ab] Yajing Li[a] and Joseph B. Herzog[a]

Surface-enhanced Raman spectroscopy (SERS) is an experimental tool for accessing vibrational and chemical information, down to the single molecule level. SERS typically relies on plasmon excitations in metal nanostructures to concentrate the incident radiation and to provide an enhanced photon density of states to couple emitted radiation to the far field. Many common SERS platforms involve metal nanoparticles to generate the required electromagnetic enhancements. Here we concentrate on an alternative approach, in which the relevant plasmon excitations are supported at a truly nanoscale gap between extended electrodes, rather than discrete subwavelength nanoparticles. The ability to fabricate precise gaps on demand, and in some cases to tune the gap size *in situ,* combined with the additional capability of simultaneous electronic transport measurements of the nanogap, provides access to information not previously available in standard SERS. We summarize the rich plasmonic physics at work in these extended systems and highlight the recent state of the art including tip-enhanced Raman spectroscopy (TERS) and the application of mechanical break junctions and electromigrated junctions. We describe in detail how we have performed *in situ* gap-enhanced Raman measurements of molecular-scale junctions while simultaneously subjecting these structures to electronic transport. These extended electrode structures allow us to study the pumping of vibrational modes by the flow of tunneling electrons, as well as the shifting of vibrational energies due to the applied bias. These experiments extend SERS into a tool for examining fundamental processes of dissipation, and provide insight into the mechanisms behind SERS spectral diffusion. We conclude with a brief discussion of future directions.

Received 20th November 2012,
Accepted 17th January 2013

DOI: 10.1039/c3cp44142c

www.rsc.org/pccp

Introduction

Raman spectroscopy is a tremendously useful tool for examining low energy excitations, including vibrational modes of molecules,[1] electronic/vibrational processes in materials of reduced dimensionality such as graphene,[2] and electronic excitations in some solid state materials.[3] In this form of inelastic light scattering, incident photons interact with an analyte *via* that system's polarizability tensor, either depositing a quantum of energy into an excitation (Stokes scattering) or acquiring a quantum of energy from an excitation (anti-Stokes scattering). Beyond the particular polarization matrix elements, the Raman scattering rate is proportional to the electromagnetic intensity at the molecule, and the density of states available for the outgoing Raman-scattered photon.

The discovery of surface enhanced Raman spectroscopy (SERS) in the 1970s[4–6] raised the possibility of using Raman emission to examine minute quantities of analytes in close proximity to metal surfaces. In SERS[7] the Raman scattering rate is strongly modified from what one would see in gas- or solution-phase experiments due to the effects of the surface. The dominant effect is the electromagnetic or plasmonic enhancement from the collective response of the electronic fluid in the nearby metal structures. Through a combination of geometry and metal dielectric function, metal nanostructures have a frequency-dependent optical response with contributions from plasmons, the normal modes of the electronic fluid.[8,9] The plasmon response involves the displacement of charge density from its equilibrium position on length scales generally small compared to the wavelength of exciting incident light. As a result, the local (near) electromagnetic field oscillating at the optical frequency can be considerably enhanced relative to that of the incident radiation, by a factor $g(\omega)$, where the magnitude and frequency dependence depend on the details of the metal composition and geometry.

[a] *Department of Physics and Astronomy, Rice University, 6100 Main St., Houston, TX 77005, USA. E-mail: natelson@rice.edu*
[b] *Department of Electrical and Computer Engineering, Rice University, 6100 Main St., Houston, TX 77005, USA*

In SERS, the local electromagnetic intensity at the incident frequency ω, enhanced by $g(\omega)^2$, interacts with the molecular polarization to drive Raman emission. The local plasmons also increase the photonic density of states at the emission frequency by a factor of $g(\omega')^2$, where ω' is the scattered frequency. In early incarnations of SERS, plasmonic "hotspots" with large field enhancements appeared serendipitously in roughened metal films. The development of both bottom-up and top-down nanofabrication methods has led to a resurgence for SERS, with more than 1000 papers about this topic in 2012 alone, according to Thomson Reuters Web of Science. Combined with increases in computational power and the availability of finite element and finite difference time/frequency domain solvers, nanofabrication and computational electrodynamics have enabled the rational design of plasmonic nanostructures for SERS.[10]

Traditionally the hotspots with the greatest SERS enhancements have been realized in nanoscale gaps between plasmonically active nanostructures.[11] For example, aggregated ensembles of metal nanoparticles naturally lead to such gaps, and these were employed in the first demonstrations of Raman spectroscopy with single-molecule sensitivity.[10,11] A simple, intuitive picture of this concept is shown in Fig. 1a, where the dipolar plasmons of two sub-wavelength metal nanoparticles are excited by light polarized along the interparticle axis, leading to an enhanced electric field in the interparticle gap. As we review in this Perspectives piece, similar large field enhancements have been demonstrated using nanogaps between *extended* electrodes (Fig. 1b) rather than discrete nanoparticles. Moreover, extended electrodes allow the application of electrostatic potentials and the simultaneous measurement of electronic transport in concert with Raman emission. These additional capabilities provide further means of determining whether Raman emission arises from a single molecule, and enable studies of current- and voltage driven phenomena that are otherwise difficult to access. These studies reveal much about the changes of junctions at the single-molecule level, as well as provide information about the evolution of the vibrational and electronic distributions under bias. A major theme of this article is the review of recent developments in these areas. We include a summary of our own group's recent results, and conclude with an outlook at future prospects enabled by the use of extended electrodes as enhanced Raman substrates. The examples discussed are meant to be illustrative rather than comprehensive, and the omission of a reference should be interpreted as an oversight rather than a critical judgment.

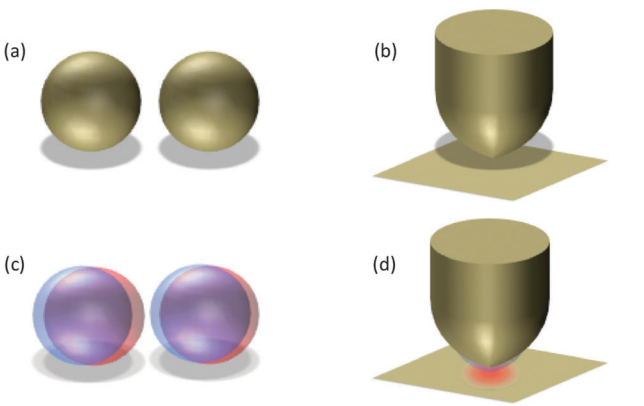

Fig. 1 Archetypal plasmonically active substrates for SERS. (a) Two subwavelength nanoparticles positioned so that they are coupled in the optical near field. (b) A metal scanned probe tip (semi-infinite) in close proximity to an underlying metal surface. (c) When an optical electric field polarized along the interparticle axis drives the coupled nanoparticles at the appropriate resonant frequency, the displacement of the electron cloud (blue) relative to the ionic background (red) leads to a greatly enhanced local electric field between the particles. (d) A nanogap plasmon resonance can exist, built from linear combinations of the delocalized surface plasmon continua of the tip and surface. Shown schematically here is a dipolar gap mode that again features greatly enhanced electric field in the nanogap region.

Plasmon modes and enhancements

To understand the differences between discrete, subwavelength nanoparticle combinations and extended electrodes, it is useful to develop an intuition for the plasmonic properties of electromagnetically coupled structures. Consider two or more plasmonically interesting (in the sense that the metal dielectric function supports plasmon excitations that are not enormously damped) nanostructures in sufficiently close proximity that they are significantly coupled *via* the optical near-field. Each of these nanostructures supports a spectrum of plasmonic normal modes. When these nanostructures are comparable in size to the plasmon wavelength, the spectrum of modes is discrete, while extended structures support a continuum of surface plasmons. In the familiar case of an ideal spherical metal particle, those modes can be described as oscillating multipoles; the common dipolar mode corresponds to the uniform displacement of the conduction electron fluid of the whole sphere relative to the ionic lattice.

Once two nanostructures are coupled *via* the optical near field, the plasmon resonances of the individual nanostructures are no longer normal modes of the coupled system. Rather, the composite system exhibits its own spectrum of plasmon resonances that can be considered as "built from" linear combinations of the subsystem modes.[12,13] If each nanostructure had a single dominant mode, one can think of the combined system having "bonding" and "antibonding" hybrid modes. Note that not every plasmon mode (of an individual or combined system) is "bright" in the sense of coupling strongly to far-field radiation. Modes without a net dipole moment tend to be "dark", though a dark mode of a subsystem can have profound consequences if hybridized with bright modes.[14]

As the distance d between plasmonic nanostructures is decreased, the enhancement of the local electric field between the nanostructures grows considerably faster than $1/d$ for hybridized plasmon modes that involve oscillating charge densities of opposite signs across the interparticle gap.[15–17] At the same time, because of the interaction, the frequency of that particular hybridized mode shifts to the red with decreasing d. Very recently, it has become possible under some circumstances

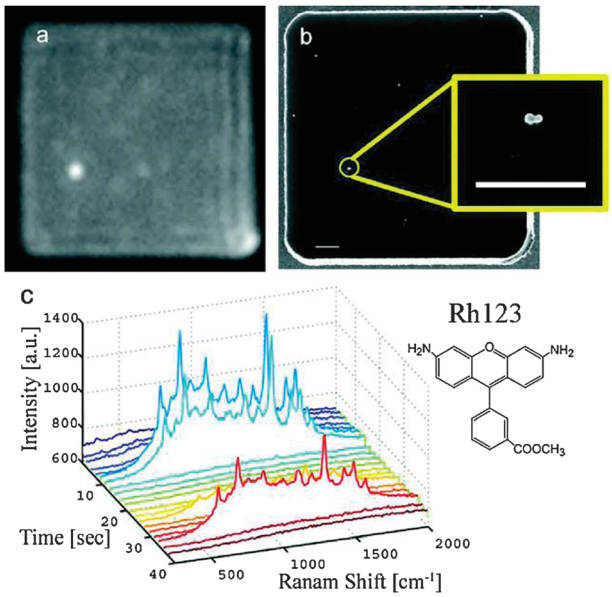

Fig. 2 An example of single-molecule SERS obtained from a nanogap between constituents of a dimer of Ag nanoparticles. (a) Raman microscope image showing a bright spot of emission. (b) Electron micrograph of the same region, showing the individual dimer linked by a single dye molecule. The scale bar is 1 μm. (c) Raman spectra as a function of time, showing blinking that is often present in single-molecule Raman. Adapted with permission from Dadosh *et al.*, *ACS Nano*, 2009, **3**, 1988–1994. Copyright 2009, American Chemical Society.

to monitor the evolution of plasmon modes as a function of interparticle separation in discrete nanoparticles through electron energy loss spectroscopy.[18]

Extremely large enhancements ideal for single-molecule SERS have been found at hotspots that are truly nanoscale (~2 nm) gaps between nanoparticles that are excited at the frequency of the mode built out of the symmetric linear combination of the dipolar resonances of those discrete nanoparticles.[11] Recent single-molecule SERS studies have taken advantage of this,[19] either through aggregation of nanoparticles[20] or through deliberate self-assembly of nanoparticle dimers linked by the molecule of interest (Fig. 2).[21]

The hybridized nature of nanogap plasmon modes becomes more obvious when considering gaps between extended electrodes. For example, a metal tip of the type used for scanning tunneling microscopy (STM) supports a continuum of delocalized, propagating surface plasmon modes over some frequency range. Likewise, a metal film supports a similar continuum. In the absence of coupling between the two, there is no additional physics. However, when the tip is brought very close to the metal film (within a few nm), tip plasmon modes of the combined system develop, localized to the nanogap region and the immediately surrounding tip and film metal.[16,17,22] Such modes have been known for decades. These tip modes can be excited by tunneling electrons of sufficient energy, and their radiative decay is responsible for the bias-driven light emission seen in STM experiments.[23] In the language of hybridization, the localized tip mode is a new normal mode of the coupled system and is ''built from'' a linear combination of the surface plasmon modes of the tip and film.[24] The dipole-active tip modes relevant to light emission experiments typically involve charge displacements of the type shown in Fig. 1b.

Extended electrode approaches to enhanced Raman scattering

The existence of nanogap modes raises the possibility of using extended electrodes for high sensitivity enhanced Raman scattering rather than aggregates, clusters, or dimers of discrete, subwavelength plasmonic nanoparticles. Extended electrodes, able to connect to external experimental apparatus, provide the opportunity to add additional modalities to Raman studies. Chief among these are scanned probe imaging, geometric adjustment of the hotspot configuration, and the controlled application of voltages and simultaneous measurement of electronic transport. These expand the scope of information available in SERS measurements, allowing new insights into the basic physical chemistry of SERS, the relative roles of plasmonic and chemical enhancements, and the flow of energy through inelastic processes at the molecular scale.

In tip-enhanced Raman spectroscopy (TERS), one electrode is a movable scanned probe microscope tip constructed from some plasmonically active metal, while the other electrode is a planar, plasmonically active metal film coated at some density with molecules of interest. Hybrid plasmon modes localized to the interelectrode gap provide the local enhancement of incident electromagnetic fields on length scales comparable to the radius of curvature of the tip. Performing scanning probe microscopy, either atomic force microscopy or STM, in tandem with TERS, makes it possible to target individual molecules or groups of molecules, provided the underlying metal surface is smooth, flat, and free of contaminants. While carbon contamination is always a concern in high sensitivity SERS,[25] combining scanned probe images of the surface with spatially resolved Raman spectra at least constrains the observed Raman emission to originate from a specific molecular-scale region (Fig. 3).

TERS with single-molecule sensitivity has recently been reported by several groups.[26–30] There has been a recent excellent review[31] that we recommend for a detailed discussion of single-molecule SERS. For our purposes, and to motivate what extended electrode techniques like TERS bring to this challenge, we briefly summarize the situation. It has been known for more than 15 years that Raman enhancements sufficient to observe single molecules are possible.[32,33] Temporal fluctuations in Raman intensity (''blinking'') and vibrational energies (''spectral diffusion'') are certainly highly suggestive, since it is unlikely that large ensembles of molecules could exhibit such phenomena synchronously. However, actually proving that Raman emission in a particular experiment originates from a single molecule is quite challenging, particularly if one must rely solely on the properties of the Raman spectra. With nanoparticle-based SERS substrates, approaches that have been taken include: dilution of the analyte to nearly homeopathic levels, so that only a very small number of

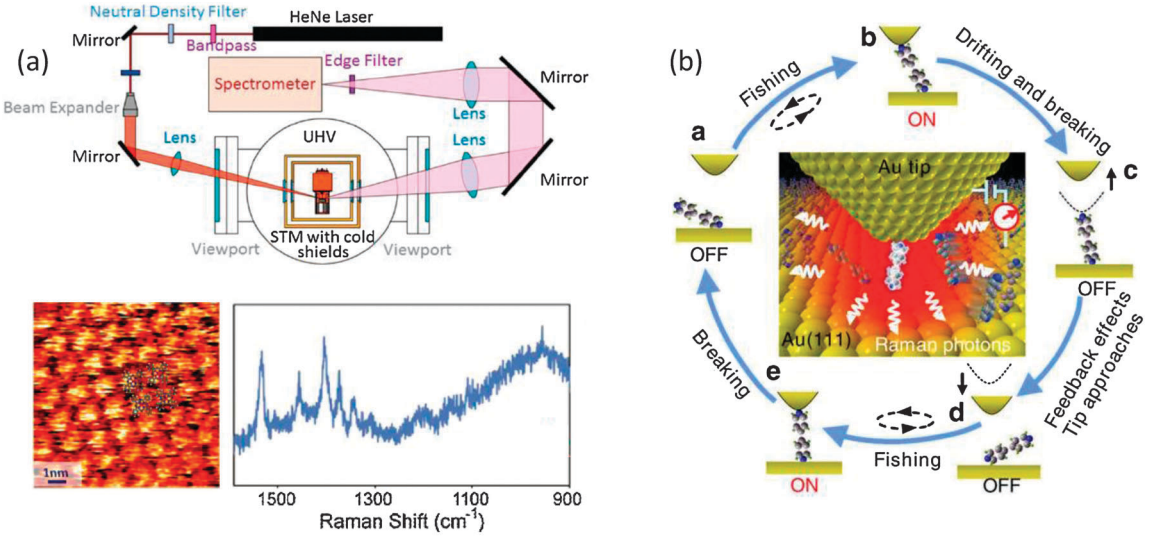

Fig. 3 Examples of tip-enhanced Raman spectroscopy, a technique that naturally uses extended metal electrodes as high sensitivity SERS substrates. (a) A schematic of an ultrahigh vacuum (UHV) approach to TERS. Lower: molecular-resolution STM image of copper phthallocyanine on Ag(111) (left) and a TERS spectrum of this molecule (right) obtained with this setup. Adapted with permission from Jiang *et al.*, *Nano Lett.*, 2012, **12**, 5061–5067. Copyright 2012, American Chemical Society. (b) A TERS approach, ''fishing-mode TERS'', designed for simultaneous TERS and single-molecule electronic conduction measurements. Reprinted by permission from Macmillan Publishers Ltd: Liu *et al.*, *Nat. Commun.*, 2011, **2**, 305. Copyright 2011.

analyte molecules can be present;[11] arguments based on statistical analyses of the blinking[32] and spectral diffusion; and bianalyte methods,[34,35] where two types of analytes are present (including isotope-tagged species[36,37]), and statistics are compiled showing the presence of one species' SERS spectrum or the other, but never both.

A major advantage of scanned probe methods, particularly those that work in ultrahigh vacuum on single-crystal metal sample surfaces,[30] is that it is possible to identify a particular target molecule for study. This reduces the probability that the emitted Raman light originates with some contaminant or extrinsic molecule. A second advantage is the ability to alter the interelectrode gap *in situ,* tuning the plasmonic enhancement. Combined with knowledge of the unenhanced cross-section for Raman emission, it is then possible to calibrate the plasmonic enhancement for comparison with computational models, or attempt to infer any chemical enhancement contribution.

The recent work by Jiang *et al.* is an excellent example of the capabilities of UHV TERS.[30] The TERS platform is a UHV STM with molecular resolution that makes use of Ag tips and a single-crystal Ag(111) surface as the substrate for molecular deposition. The investigators employ resonant Raman with a 632 nm excitation wavelength to study copper phthallocyanine molecules assembled into monolayers on the Ag(111) surface. From the tip–surface distance dependence of the Raman signal, they obtain an estimate of plasmonic TERS enhancement of 7.1×10^5, sufficient for single molecule detection in the resonant Raman limit.

This experiment, a tour de force combining UHV surface science capabilities with optical excitation and detection, highlights a major challenge of TERS work: Because of the tip-planar sample geometry, optimal coupling of light into and out of the junction is not simple. Recent advances have explored the use of resonant gratings on the sides of the metal tip to improve in-coupling of far-field excitation.[38] High laser intensities can also lead to heating of the tip, which often has a weaker thermal connection to the ambient temperature than the sample substrate.

By combining both scanned probe imaging and measurements of electronic conductance,[29] claims of single-molecule TERS sensitivity can be placed on a firmer footing than those that employ imaging and Raman emission alone. Repeated breaking and formation of tip–surface junctions with continuous measurements of tip–surface conductance can be used to compile a histogram of conductance values[39] and to identify the conductance contribution of individual molecules.[40,41] In their ''fishing-mode TERS'' experiments,[29] Liu *et al.* use the measured tip–surface conductance to determine when the tip–surface junction is bridged by a single molecule of 4,4′-bipyridine, and record the Raman emission as a function of time. In this way they are able to correlate the observed Raman spectra with the measured conductance and compare with density functional calculations. Central to the interpretation of the resulting data as single-molecule Raman spectra is the idea that tip–surface electronic conduction takes place through quantum mechanical tunneling, an exponentially localized process; since the tunneling conductance probes only a molecular-scale volume, clear correlations between the Raman spectra and the measured conductance (either as a function of time or as a function of some tuning parameter) imply that the dominant Raman emission originates from that same volume.

Mechanical break junctions

Some investigators have opted to leverage this local character of the tunneling conductance by creating *planar* extended electrode structures supporting nanogap plasmon modes for

SERS. Planar junctions can be more readily integrated into Raman microscope setups that allow for normal incidence and collection of light *via* standard microscope objectives. Large-area molecular junctions have been examined to detect bias-driven chemical changes in molecular layers.[42,43] Edges of wide metal strips have been used,[44] but more commonly the attempt is made to recreate, in planar form, electrodes that taper to a tip-like geometry.

An early attempt to combine the adjustability of TERS with the ease of optical access and transport capabilities inherent in planar device designs was implemented by Tian *et al.*,[45] who incorporated a flexure-based mechanical break junction as their Raman substrate of choice. A lithography-defined, flexure-based mechanical break junction is shown schematically in Fig. 4a. Electrodes bridged by a narrow constriction are fabricated through e-beam lithography on a polyimide layer coating a flexible substrate. The constriction is suspended through oxygen plasma-based etching, and the substrate is mounted so that it may be flexed by a controlled pusher pin. Thanks to this geometric arrangement, there is a significant mechanical advantage, so that micron-scale motion of the pusher pin translates into sub-nanometer changes in the interelectrode separation. This arrangement is very stable against vibrational perturbations. Integration of this apparatus into an optical cryostat with a short optical working distance is challenging but possible.

In measurements reported in this geometry with Au electrodes, Tian *et al.* find readily detectable Raman enhancement at the interelectrode gap, with increasing signal for closer interelectrode separations. This is an important result highlighting the potential for this approach, which can readily be integrated with electronic transport measurements. However, the total Raman signal at the gap is only about 10× what is seen when the laser spot is directly over one of the pads. Considerably greater enhancements are possible in similar geometries with Au electrodes; in this case the use of a 632 nm excitation source is likely the issue, as the Au interelectrode gap modes in other experiments appear to be closer to resonance when excited at 785 nm.

Very recently, Konishi *et al.* have performed[46] gap-enhanced Raman measurements in Au break junctions combined with single-molecule electronic conductance measurements. With an excitation wavelength of 785 nm and immersing the junction and microscope objective in water, the authors performed measurements *in situ* in solution, looking at molecules of 4,4′-bipyridine. Similar in spirit to the fishing-mode TERS experiments,[29] Konishi *et al.* carefully analyze the variety of Raman spectra that are presented when their break junctions are in configurations with conductances that match the expected single-molecule conductance. They find that the relative intensity of particular Raman modes appears to depend

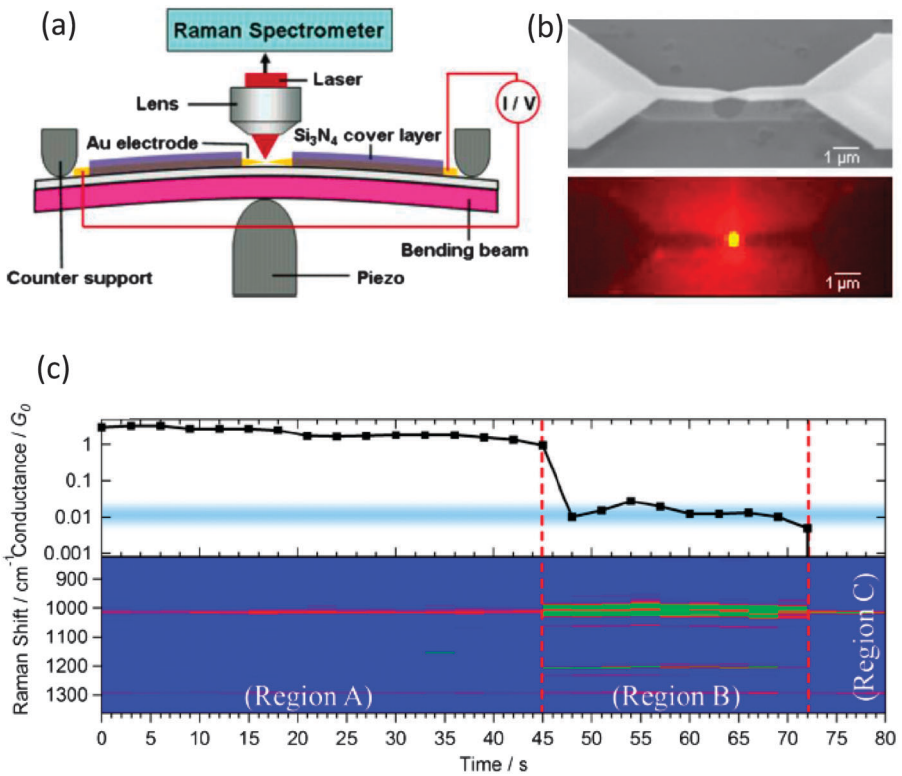

Fig. 4 Mechanical break junctions for gap-enhanced Raman scattering. (a) A diagram of a mechanical break junction integrated with a Raman microscope. Adapted with permission from Tian *et al.*, *J. Amer. Chem. Soc.*, 2006, **128**, 14748–14749. Copyright 2006, American Chemical Society. (b) Electron micrograph and Raman microscope image (785 nm excitation) of a Au break junction containing 4,4′-bipyridine. (c) Source–drain conductance (top) and SERS emission (bottom) as a function of time for the device in (b). The strong correlation between SERS and conductance strongly implies that single-molecule Raman response is being observed. Adapted with permission from Konishi *et al.*, *J. Amer. Chem. Soc.*, 2012, advanced online publication. Copyright 2012, American Chemical Society.

on the molecular orientation within the nanogap, as does the conductance. Comparisons with density functional calculations show consistency with this picture, emphasizing that the SERS spectrum depends upon the polarizability tensor of the entire molecule/metal region.

Electromigrated and self-aligned junctions

Lithography followed by electromigration provides an alternative route to plasmonic nanogaps between extended source and drain electrodes. This method for fabricating nanometer-spaced junctions has its origins in the electronic transport community, where it was first applied to create electrode sets appropriate for the measurement of transport through individual semiconductor nanocrystals.[47] This approach has since been employed by many groups to examine electronic transport in single molecules.[48–55] The advantages of the electromigration approach are its compactness (no moving parts; easy to integrate into a standard optical cryostat) and the ability to integrate an underlying third electrode to serve as a gate, permitting capacitive shifting of a molecule's electronic levels relative to the Fermi level in the source and drain electrodes.

This method is based on the momentum transfer between current-carrying electrons and the atoms at the scattering sites responsible for limiting the resistivity. Atoms at defects, surfaces, and grain boundaries take up the recoil from scattering the conduction electrons, and this can lead to preferential motion of those atoms, with rates enhanced at higher lattice temperatures thanks to the activated nature of atomic diffusion. A lithographically defined constriction between Au electrodes is subjected to a computer-controlled voltage bias. The current density is largest at the constriction, favoring electromigration. A local reduction in constriction width increases the local current density, leading to a tendency toward run-away and pinch-off of the constriction into two distinct (source and drain) electrodes. Conductance jumps on the order of the quantum of conductance, $G_0 = 2e^2/h$, are seen as the constriction approaches the atomic scale. With care and practice, it is possible to achieve yields greater than 90% of nanogaps close enough to permit interelectrode tunneling conduction. When the intent is to study molecules, this process is most often performed in the presence of a molecular layer (either spin-cast or deposited *via* self-assembly) prior to electromigration. Local heating due to electromigration can be significant particularly in refractory metals; while this is considerably less in gold junctions, it is worth some concern about whether molecules of interest will survive, undamaged, on the metal surface through the migration process.

These structures have certain advantages and disadvantages when applied for single-molecule studies. The exponential decay of tunneling probability with distance ensures that, unless the tips of the resulting electrodes are very blunt, the interelectrode conductance is dominated by a molecular-scale volume, reminiscent of the situation in scanning tunneling microscopy. This explains their efficacy in single-molecule electronic transport studies. However, this also implies that the interelectrode conductance is sensitive to atomic-scale displacements of surface atoms. Moreover, the metal configuration immediately after electromigration is likely a metastable arrangement of atoms, since it is the result of a nonthermal, nonequilibrium process. As a result, the interelectrode conductance near room temperature is known to fluctuate as a function of time as well as generally trend downward, typically falling below measurable limits over timescales of tens of minutes. Note, too, that this technique does not control the crystallographic orientation of the final metal surfaces; given that work functions can vary by fractions of a volt depending on crystal orientation, this leads to inherent variability in the resulting transport properties. To minimize the risk of surface contamination by unintended adsorbates, electromigration is best performed in cryopumped ultrahigh vacuum conditions. When these are not attainable, it is important to be aware that there is therefore some risk that measurements will be influenced by adsorbed impurities or gaseous contaminants in the environment (*e.g.*, oxidative photobleaching due to trace oxygen levels). We note that electromigrated junctions can possess strong SERS hotspots even when the closest interelectrode separation is too large to permit measurable tunneling conductance.[56,57] Finally, we point out that conductance in electromigrated junctions can, depending on the geometry, include a significant direct tunneling contribution as well as the component of the current that traverses the molecule. Hence junction conductances can be higher than those seen in elongated mechanical break junction experiments where the molecular contribution is expected to dominate.

Recently a self-aligned technique[58] has been demonstrated to successfully fabricate plasmonically-active nanojunctions with[59] and without[60] extended electrodes. This fabrication method allow for mass production of large arrays of devices with only two lithography steps. An example of a resulting electrode set is shown in Fig. 5. The first electron beam

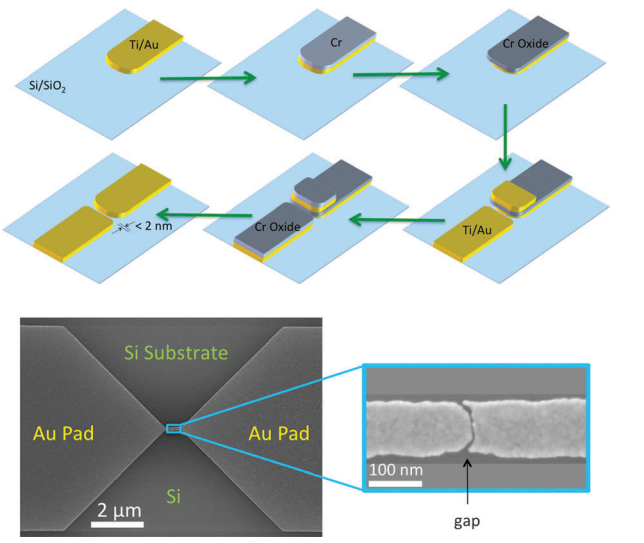

Fig. 5 The self-aligned nanogap process. Top: process flow. Bottom: an example of a self-aligned nanogap between two extended electrodes. Electromigrated junctions look rather similar but can only be produced one at a time. This self-aligned process produces nanogaps smaller than a few nanometers, with the strongest SERS emission coming from the smallest non-shorting nanogaps.

lithography (EBL) step patterns one side of the junction on a Si substrate with 200 nm of thermal oxide. Next, 1 nm of Ti, 15 nm of Au, 1 nm of SiO_2, and 12 nm of Cr are evaporated over the developed resist. The Ti layer is an adhesion layer, the Au layer is the plasmonically active metal, the SiO_2 is a diffusion barrier to prevent Cr from diffusing into the gold, and the Cr is a sacrificial layer key in the self-aligned process. After evaporation the sample is exposed to air which oxidizes the Cr causing it to expand a few nanometers creating a Cr-oxide ledge extending out beyond the lower layers. This ledge is critical to the self-alignment process by acting as a shadow mask in the subsequent evaporation. After standard liftoff processing, a second and final EBL step patterns the other half of the junction, intentionally overlapping it with the previous pattern. Once development is complete, the same layers are evaporated again, and during this evaporation the Cr-oxide ledge from the first step now acts as a shadow mask to self-align the two Au structures so that they end up only a few nanometers apart, creating the nanogap. The gap is now present underneath Cr-oxide and other sacrificial layers, therefore, a Cr etch is used to remove all of these layers, and finally, the SiO_2 diffusion barrier is no longer needed and is etched away with a quick buffered oxide etch. When the etching is finished, the samples are now completed and ready for molecular self-assembly. Molecule types can vary, as gap-enhanced Raman scattering has been able to detect many different types of molecules.

These self-aligned gaps have proven to be considerably more robust than electromigrated structures, with nanoscale junctions acting as Raman hotspots for months.[59] We believe that this longevity results from the relaxed metal structure of these junctions compared with the metastable metal configurations produced by electromigration. Electron microscopy examinations of ensembles of self-aligned junctions clearly show the steep dependence of plasmonic enhancement with interelectrode separation.

The recent studies of large ensembles of self-aligned junctions have also shown that these particular structures, and their isogeometric electromigrated equivalents, have unusual hotspots compared to the standard dipolar tip plasmons described above. Most prior experiments have found maximum enhanced Raman signals when the (normally) incident electric field is polarized along the interelectrode axis (across the nanogap).[45,46,57] In contrast, in our experiments we find that the enhanced Raman signal is maximized when the incident electric field is polarized transverse to the interelectrode axis (parallel with the nanogap).[59] Cathodoluminescence measurements and finite-element electromagnetic simulations explain that this surprising polarization dependence stems from the particular plasmon modes with the greatest enhancements. There is a strong, dipole-active transverse plasmon resonance of the nanowire active at the incident 785 nm wavelength. When there is an asymmetric nanogap in the wire, this mode hybridizes with highly localized, multipolar (and therefore optically "dark") modes at the nanogap. These results demonstrate that plasmon engineering beyond simple dipolar tip modes is possible in extended electrode structures, and that capturing the essential plasmon physics requires computational models with realistic broken symmetries.[59]

Transport measurements in electromigrated gaps

For simultaneous transport/Raman experiments, we examine the gap-enhanced Raman response of electromigrated junctions using 785 nm excitation. Initial investigations were performed using a commercial Raman microscope (WiTec) in ambient air, using junctions electromigrated prior to placement in the microscope field of view, and without any electronic transport investigations.[56] In later studies, electromigration was performed *in situ* in the Raman microscope setup, to minimize delays and to permit simultaneous electronic transport measurements during the Raman data acquisition.[61] Finally, with the completion of a custom Raman microscope and acquisition of a microscope cryostat and vacuum system, we made the transition to performing electromigration and subsequent measurements in vacuum and at substrate temperatures of 80 K.

As shown in Fig. 6, we clearly observe enhanced Raman emission localized to a focus-limited spot centered on the

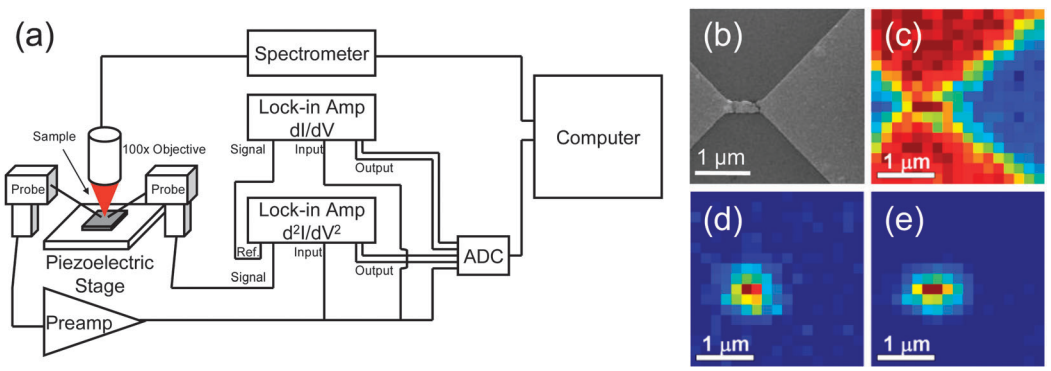

Fig. 6 Gap-enhanced Raman and electronic measurements with electromigrated gaps. (a) Measurement scheme. (b) Electron micrograph of an electromigrated nanogap. (c) Raman microscope map of Si Raman emission, clearly showing where Si line is attenuated by presence of Au pads. (d, e) Raman emission, localized to a diffraction-limited spot around the nanogap. In (d), integrated Raman emission of the 1590 cm^{-1} carbon ring mode of *para*-mercaptoaniline; in (e), the integrated low-wavenumber electronic Raman continuum. From Ward *et al.*, *Nano Lett.*, 2008, **8**, 919–924. Copyright 2008, American Chemical Society.

interelectrode gap. Raman response of self-assembled molecules is undetectably weak on the large Au pads, even with long (tens of seconds) integration times. Likewise, unmigrated junctions show no detectable Raman signal. Junctions with no intentional molecular coating migrated and measured in ambient air showed pronounced Raman emission from the junction within seconds of electromigration. The spectra showed broad emission with irregular peaks between 1000 cm^{-1} and 1600 cm^{-1}, consistent with spectra identified as carbon contamination,[62] as well as extremely large temporal fluctuations.

Junctions coated with a self-assembled monolayer (SAM), however, usually exhibit Raman emission consistent with expectations from the molecule of interest, even when subsequently measured under ambient conditions. This is consistent with the extremely local character of the plasmonic hotspot in these structures: When a SAM is present, air contaminants cannot infiltrate the hotspot region.

Simultaneous transport and Raman measurements use lock-in amplifier techniques synchronized with CCD spectrometer readout. A small ac voltage bias, V_{ac}, at frequency ω is added to a dc bias, V_{dc}, through a summing amplifier, and applied to the drain electrode, while the source electrode is connected to a current preamplifier. The output of the current amplifier is read directly using a data acquisition system (DAQ) and fed into two lock-in amplifiers, one measuring at ω (to determine dI/dV) and a second measuring at 2ω (to determine d^2I/dV^2).

Transport in these experiments is non-resonant, as shown in Fig. 7a and b. That is, the highest occupied and lowest unoccupied molecular orbitals (HOMO and LUMO, respectively) do not fall in the "bias window" defined by the chemical potential difference between the source and drain electrodes, eV. In this regime, the molecule acts as an effective tunneling barrier for electrons.[63] Charge is transported through second-order tunneling processes ("cotunneling" in the language of condensed matter physics; "superexchange" in the language of physical chemistry), where the LUMO (HOMO) acts as a virtual intermediate state for electron (hole) transport. Note that this transport mechanism leaves the average charge on the molecule *unchanged*. Therefore, in this regime one does not expect to see alterations in the Raman spectrum due to fluctuations in the redox state of the molecule. We return to this issue below.

The short-range tunneling nature of transport provides an extremely useful diagnostic for the sensitivity of simultaneously performed SERS measurements. Two examples are shown in Fig. 8. In single-molecule junctions, either electromigrated[61] (Fig. 8a) or mechanical break junctions[46] (Fig. 8b), the tunneling conductance interrogates only a molecular-scale volume, as in STM. Stochastic variations in that tunneling conductance correspond to molecular reorientations, molecular diffusion, or other

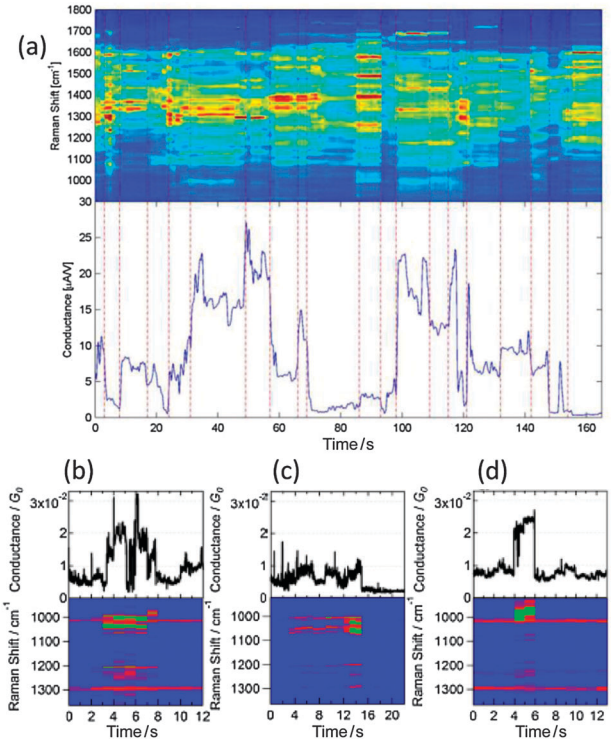

Fig. 8 Conductance *vs.* time coinciding with Raman emission *vs.* time. (a) Raman emission (top) and conductance as a function of time from a junction containing oligophenylene vinylene molecule(s). Adapted from Supplementary Information, Ward *et al.*, *Nature Nano.*, 2011, **6**, 33–38. Reprinted by permission from Macmillan Publishers Ltd., Copyright 2011. (b) Conductance (top) and Raman emission *vs.* time in mechanical break junctions containing 4,4′-bipyridine molecules, in a conductance range consistent with single molecules. Adapted with permission from Konishi *et al.*, *J. Amer. Chem. Soc.*, 2012, advanced online publication. Copyright 2012, American Chemical Society.

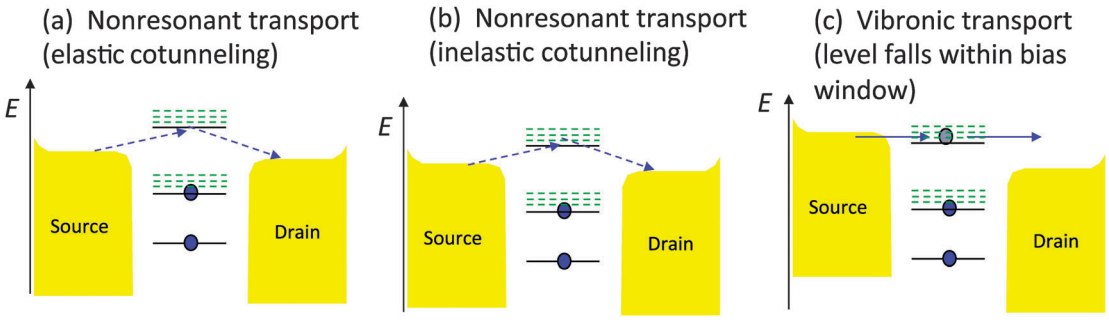

Fig. 7 Electronic transport processes. (a) Off-resonance transport *via* a second-order tunneling process – elastic cotunneling or superexchange. (b) Inelastic cotunneling, where the electron tunnels onto the vibrational ground state of the molecule and off the vibrational excited state, leaving behind a vibrational quantum of energy. (c) At higher bias, vibronic transport, directly through vibrationally excited states.

changes in the electronic environment (effective barrier height) of the critical tunneling volume. These conductance changes are strongly correlated in time with corresponding alterations in the Raman spectra. The simplest interpretation of such correlations is that the Raman emission originates from the molecular-scale volume probed by the tunneling conductance. Indeed, in the work[46] of Fig. 8b, electronic structure calculations are performed to try to infer the particular molecular conformations that correspond to both the conductance and Raman data. In principle the precise enhanced Raman spectrum (spectral positions and relative intensities) depends on the detailed junction configuration, through the polarizability tensor of the whole molecule + junction region. However, extracting such information is computationally extremely challenging at present. From the Raman spectra alone it would be difficult to argue that these experiments have achieved single-molecule sensitivity, while such a conclusion becomes the natural one when the exponentially local aspect of tunneling transport is added to the SERS data.

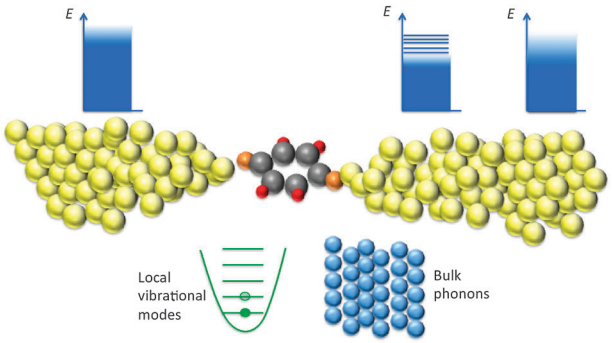

Fig. 9 A junction driven out of equilibrium. Electrons tunnel from the left electrode to the right, *via* a molecule. Near the molecule, the electronic distribution is nonthermal because ''hot'' electrons arrive at elevated energies due to the applied bias. On the scale of the electron–electron inelastic scattering length away from the junction, the electrons arrive at an effective temperature, and eventually thermalize with substrate phonons. If the tunneling electrons have sufficient energy, they can excite local vibrational modes, which relax at some rate to the substrate phonons.

Transport – inelastic effects and SERS

Associated with each molecular electronic level is a manifold of vibrational states with characteristic energies $\hbar\omega_i$. In non-resonant transport, when the bias energy scale eV exceeds the vibrational energy $\hbar\omega_i$, an additional transport channel becomes accessible, as shown in Fig. 7b. In this inelastic cotunneling process, an electron tunnels onto the vibrational ground state of the molecule and off the vibrationally excited state of the molecule, leaving behind a vibrational quantum of energy. The rate of this process depends on both the electron–vibrational coupling for that mode, and the Franck–Condon factors that determine the electronic overlap between the vibrational ground and excited states. This process is the physical basis for inelastic electron tunneling spectroscopy. In IETS, electronic excitation of vibrational modes is detected by its impact on the electronic current. The total conductance results from the coherent interference of elastic and inelastic tunneling contributions.[64] Depending on the relative phases of the two contributions, the onset of inelastic tunneling shows up as a feature (a peak, a dip, or a Fano line shape) in d^2I/dV^2 at $eV = \hbar\omega_i$. IETS research underwent a resurgence with the advent of the STM and the ability to look at inelastic electron tunneling in a spatially resolved way through single molecules.[65]

There is a general qualitative understanding of what happens when a voltage bias is applied across such a nanoscale junction.[66] As shown in Fig. 9, the bias shifts the electronic chemical potential of the source relative to the drain, and a steady state current flows, proportional to the quantum mechanical transmittance of the junction. Electrons transmitted from the source into the drain arrive with energies above the local chemical potential, meaning that the local electronic population in the metal is no longer described by a simple, thermal Fermi–Dirac distribution. On a length scale given by the electron–electron inelastic scattering length, the electrons in the metal thermalize, with some elevated effective electronic temperature. On a longer scale, the hot electronic distribution loses energy to the bulk phonons, potentially elevating the phonon effective temperature above the equilibrium T of the substrate. If processes like inelastic electron tunneling are permitted, the tunneling electrons dump energy at some rate into local vibrational excitations of the junction. Those local vibrational modes in turn lose energy by coupling to the bulk phonons. In steady state the local vibrational occupation numbers arrive at whatever nonthermal value is required such that the rate at which the tunneling electrons pump energy into the vibrational modes is balanced by the rate at which those modes lose energy to the bulk phonons.

Combining gap-enhanced Raman and transport in single-molecule junctions finally provides an experimental handle that can give comparatively direct access to the local vibrational and electronic distribution functions. By integrating and synchronizing Raman spectroscopy with transport measurements, we can examine the evolution of the Raman spectrum as a function of bias and therefore current.

Since the anti-Stokes Raman process removes a vibrational quantum of energy from a mode, the intensity of the anti-Stokes process provides a measure of the vibrational occupation of that mode. In thermal equilibrium at temperature T, the ratio of anti-Stokes to Stokes SERS emission would be expected[44] to have the form $(g^2(\omega_{AS})/g^2(\omega_S))(\sigma_{AS}/\sigma_S)(\omega_{AS}/\omega_S)^4 \exp(-\hbar(\delta\omega)/k_BT)$. Here g is the plasmonic field enhancement, at the Stokes (anti-Stokes) scattered frequency, ω_S (ω_{AS}) respectively; σ_S (σ_{AS}) is the unenhanced Stokes (anti-Stokes) cross-section; and $\delta\omega$ is the Raman shift (vibrational frequency) of the relevant vibrational mode. The Boltzmann factor expresses the relative occupation probability of the first excited vibrational state, assuming that is the only relevant level.

In an ideal situation this allows us to define some effective vibrational temperature, T_{eff}, for any given vibrational mode based on the anti-Stokes/Stokes intensity ratio. This T_{eff} is really a proxy for the relative occupations of the vibrational ground state and first excited state, and does not necessarily indicate a

true thermalization of the molecular vibrational modes; different modes could have different T_{eff} values. As the bias conditions are varied, we can look for changes in T_{eff} as a means of inferring the current-driven heating of ionic degrees of freedom.

In practice, the analysis of real data can be considerably more challenging. In general the plasmonic enhancement's frequency dependence, $g(\omega)$, is not known, nor are the true Stokes or anti-Stokes cross-sections. There are inherent challenges in the acquisition of such data. For example, for a mode with vibrational energy of 1000 cm^{-1} at a temperature of 80 K, the Boltzmann factor alone is $\sim 5 \times 10^{-7}$, implying that even with a large number of detector counts at the Stokes shift, the anti-Stokes emission may be undetectably small. Moreover, there can be backgrounds that superpose on the Raman spectra, making clear evaluation of emission intensities difficult. One well-known background is molecular fluorescence, though this may be avoided with proper choice of excitation wavelength.

Continuum Raman emission at low wavenumbers is more difficult to ameliorate. This is believed to result from Raman scattering by electron–hole excitations in the plasmonically active metal.[11,67–71] Its extent in Stokes shift is sensitive to the disorder in the metal,[70] so that the background is nonuniversal. Anti-Stokes continuum emission can only take place using the population of electrons excited above the metal Fermi level. Therefore, the anti-Stokes continuum is expected to be proportional to a convolution of the high-energy tail of the Fermi–Dirac distribution function and a disorder-dependent function. While this background makes determination of vibrational Raman intensities challenging, it does provide experimental access to the electronic distribution function, and therefore the electronic temperature, at least for those conduction electrons directly relevant to the plasmon-enhanced Raman emission.

Fig. 10 shows a particularly clear example of the kind of data that may be obtained using extended electrodes. This data originates from an electromigrated junction of zero-bias conductance $\sim 0.65\ G_0$ containing C_{60} at a substrate temperature of 80 K. The anti-Stokes Raman spectra are shown as a function of dc bias across the junction. Rather than attempt to extract an effective temperature, as has been done previously,[44,72] we present the raw anti-Stokes counts for 3 second integration times. As the bias is increased, anti-Stokes peaks appear and become stronger. In particular, the count rates for peaks near 1147 cm^{-1} and 1264 cm^{-1} do not rise noticeably above the background until the dc bias exceeds thresholds of approximately 140–150 mV, with a larger threshold value for the higher energy mode. These energy scales are very close to the criterion $eV = \hbar(\delta\omega)$. This same thresholding property was reported previously in devices made with other small molecules, and is highly suggestive of current-driven vibrational pumping. We note that this threshold behavior appears to hold for the lower wavenumber modes as well, though the presence of the continuum background makes it difficult to make a strong statement.

A further point in favor of current-driven vibrational pumping, as opposed to simple, uniform heating of the device, is found by comparing the anti-Stokes emission with the simultaneously acquired Stokes spectra. Note that the Stokes spectrum shows a larger number of modes than the high bias anti-Stokes limit. If the anti-Stokes counts resulted from uniform device heating, one would expect anti-Stokes emission from all the Stokes modes; instead, only a subset of those modes seems to experience bias-driven activation. Data such as these provide a wealth of information about the evolution of steady-state vibrational populations when driven out of equilibrium.

Open questions remain

As we have seen, gap-enhanced Raman substrates with extended electrodes are versatile research tools, allowing the application of controlled electrostatic potentials and the simultaneous measurement of Raman emission and electronic conduction. These studies have extended our understanding of enhanced Raman at the single-molecule level and offer opportunities to study previously inaccessible physics and physical chemistry. Topics that lend themselves to future study include:

The nature of chemical enhancement

There are multiple potential sources of chemical enhancement of the Raman signal.[73] Chemical bonding to the metal surface

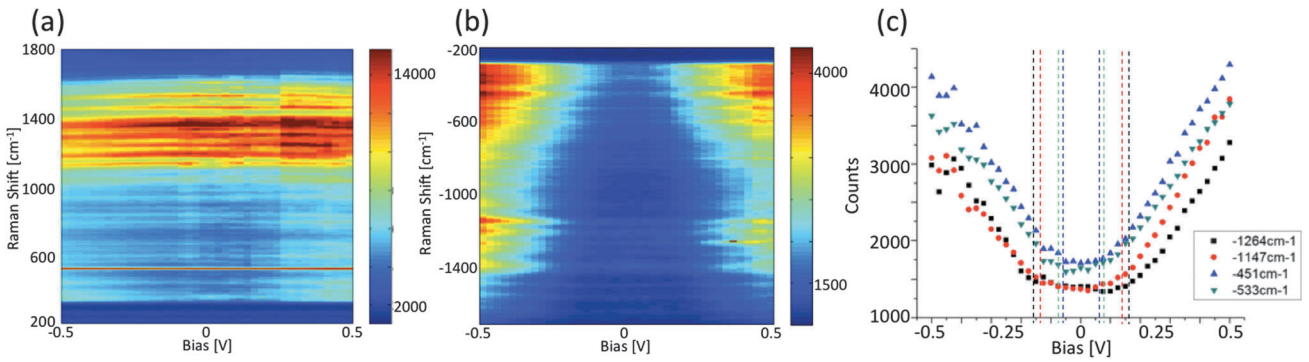

Fig. 10 Bias-driven heating in a C_{60}-containing junction. (a) Stokes Raman spectra as a function of source–drain bias. (b) Simultaneously acquired anti-Stokes spectra. (c) The raw counts of particular anti-Stokes peaks as a function of bias. Vertical dashed lines color-coded to the particular modes indicate the threshold $eV = \hbar(\delta\omega)$. Data were acquired at 80 K with 3-second integration times at each bias voltage.

and other molecule–metal interactions (*e.g.*, charge transfer; image charge alterations of the molecular charge distribution; molecular alterations to the metallic charge distribution) can modify the polarizability tensor of the molecule away from what one would find in gas-phase measurements. One potential source of chemical enhancement is a direct change in Raman cross-section due to such effects. Image charge effects can also lead to strong renormalization of the HOMO–LUMO gap of the molecule; at a given incident wavelength, this can change the proximity of the molecule to the resonant Raman condition, again leading to a chemical enhancement. Finally, depending on the energetic alignment of the molecular levels and the Fermi level of the metal electrodes, there can be a resonant contribution when the photon energy equals the energy difference between the metal Fermi level and either the HOMO or LUMO.[74]

Extended electrode approaches can potentially distinguish these possibilities. Scanned probe TERS can identify particular molecular orientations on working surfaces for comparison with detailed density functional calculations regarding molecular binding and orientation.[75,76] In adjustable systems (TERS, mechanical break junctions), it should be possible to perform gap-enhanced Raman measurements as a function of electrode separation with the molecule bound to one surface. Tuning the electrode distance systematically varies both the metal plasmonic response and the screening environment of the molecule, which again may be compared with detailed calculations. In gate-able configurations analogous to those used in single-molecule transistor experiments, electrostatically shifting the molecular levels relative to the metal Fermi level can test for resonant contributions.

Finally, while not directly related to the chemical enhancement, the ability to manipulate molecular energetics through electrostatics can allow the detailed study of vibrational energies as a function of molecular redox state. In single-molecule transistor structures, it has been possible to use the gate voltage to add or remove an electron from the molecule, with the compensating charge required to stabilize the resulting cation/anion provided by the gate electrode.[48,50,51,54,77–80] It would be very interesting to monitor the evolution of vibrational states as redox transitions are approached, when, *e.g.*, the vibrational energy scale becomes comparable to the energy difference between the Fermi level of the metal electrodes and the HOMO or LUMO. Hints of this evolution have been seen in transport measurements.[53,79] In this situation (rather than the off-resonant transport examined previously), when the redox state of the molecule is altered either in steady state or transiently, it should be possible to see the effects of molecular charging events on the Raman spectrum.

Electron–vibrational couplings, transport, and heating

As explained above, the ability to perform simultaneous Raman and electronic transport measurements permits new insights into the nature of heating and dissipation at the nanometer scale. The measurements performed so far use the current-driven vibrational response as measured through anti-Stokes Raman to infer a combination of inelastic energy loss from the tunneling electrons and relaxation of the local vibrational modes to the bulk phonons of the substrate. Further combinations of transport and Raman measurements can better untangle this convolution. Simultaneously performing IETS (looking at the impact of electron–vibrational energy transfer on the transporting charge carriers) and anti-Stokes-based Raman heating should allow a quantitative determination of both the electron–vibrational coupling for specific modes and therefore an inference of the relaxation rate of local vibrations to the bulk phonons.

Similarly, measurements thus far have operated in the off-resonant (inelastic cotunneling) transport regime. However, prior studies in both scanning tunneling microscopy[81–83] and single-molecule transistors[49,50,52,54] have clearly shown that transport may proceed through vibrationally excited states in the sequential or resonant tunneling regimes as well. In this limit the vibrationally excited state lies within the bias window, *eV*. This implies that the source–drain bias is sufficient to alter the average charge on the molecule by one electron, and further to overcome the vibrational energy threshold of a particular mode. It has been demonstrated that it is possible to transport charge through not just the first vibrationally excited state of a particular mode, but higher vibrational occupation states as well.[50,81–83] If this regime can be achieved in a SERS-accessible geometry, then it may be possible to watch the evolution of the vibrational distribution when energy is deposited by the electrons into selected vibrationally excited states.

The electronic SERS continuum

The electronic continuum mentioned previously is very much worthy of further investigation. Its origin is thought to lie with Raman scattering by the conduction electrons of the plasmonically active metal.[11,67] Recent theoretical investigations[84,85] argue that this background and its bias dependence may in fact reflect interactions between the electrons and adsorbed Raman active molecules. Further experiments in UHV environments and with tunable electrode geometries such as those in mechanical break junctions may be able to resolve the respective contributions of molecule-mediated and direct electronic heating processes. The traditional Landauer–Büttiker picture of quantum conduction, widely adopted in treatments of electronic transport through nanoscale systems, assumes no bias-driven electronic heating near the junction. It is important to establish the limits of validity for this assumption, and the electronic continuum in molecule-free junctions may provide experimental access to this question.

Other bias-driven effects – vibrational Stark physics

In addition to bias-driven vibrational excitations as seen through anti-Stokes Raman, Fig. 11 shows evidence of another interesting piece of physics, the vibrational Stark effect.[86,87] In a semiclassical interpretation of ordinary vibrational Stark physics, an applied dc electric field polarizes the molecule such that the weakly nonlinear vibrational modes are stretched, altering their vibrational energies. As is apparent from the color maps, the vibrational energies of the strong SERS-active modes systematically shift toward lower wavenumbers in a

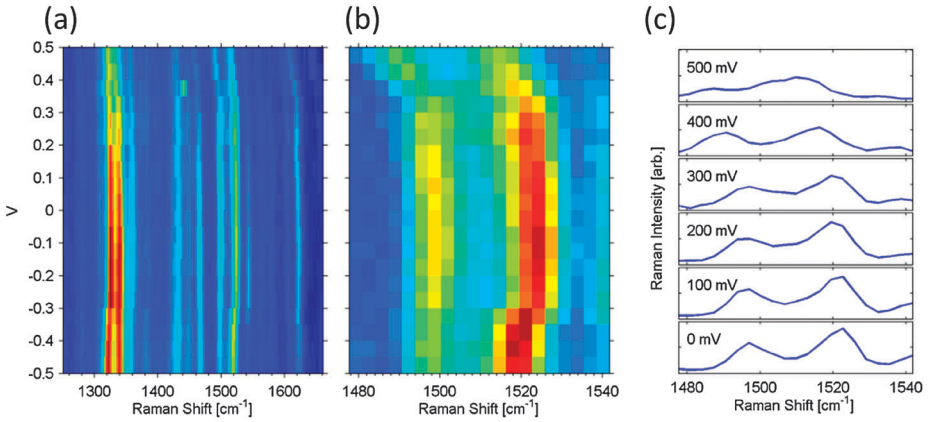

Fig. 11 Vibrational Stark physics. (a) Stokes Raman spectra as a function of source–drain bias for an oligophenylene vinylene molecule junction. (b) Zoomed and rescaled data from (a), more clearly showing the systematic variation of vibrational energy as a function of bias. (c) Line cuts through the data at particular bias values. Reprinted by permission from Macmillan Publishers Ltd: Ward *et al.*, *Nature Nanotechnol.*, 2011, **6**, 33. Copyright 2011.

trend approximately quadratic in dc bias. It remains to be seen whether these changes are in accord with theoretical expectations for vibrational Stark shifts, which should be calculable through standard electronic structure methods. Direct comparisons with theory can in principle reveal the charge state of the molecule in question, molecular orientation relative to the surface, and the effective interelectrode separation. Nontrivial changes in mode structure at high bias, such as mode splitting,[45] remain to be understood.

Conclusions

Extended electrode structures incorporating nanogaps provide additional functionality for surface-enhanced Raman studies beyond acting purely as plasmonic substrates. These nanogap systems support plasmon modes that manifestly result from hybridization of plasmonic continua in the extended electrodes. In tip–surface systems like those used for TERS, the ability to image the surface through scanned-probe techniques makes it possible to perform single- or few-molecule studies without relying on indirect or statistical arguments. Combining electronic transport measurements with enhanced Raman scattering, only possible in extended electrode configurations, similarly leverages the extremely local character of electron tunneling to probe single-molecule Raman response, and permits additional comparisons to theoretical descriptions of molecule–surface interactions. Working at comparatively high biases (tens to hundreds of mV) in planar junctions with conductances above 0.01 G_0, we have been able to use the bias evolution of anti-Stokes gap-enhanced Raman emission to examine vibrational and electronic heating driven by the current. Thresholding and mode selectivity observed in anti-Stokes Raman modes supports current-driven vibrational pumping, as opposed to simple, uniform heating of the ionic degrees of freedom of the junction. Extended electrode structures can support various hybridized nanogap plasmons, from simple dipole-active tip modes to more complex multipolar resonances accessible due to broken geometric symmetries.

Extended electrodes with nanogaps provide a platform for addressing remaining open questions in enhanced Raman spectroscopy and fundamental nanoscale processes, as described above. A common thread that has run throughout this discussion is the comparison of experimental results with theoretical expectations. Computational electrodynamics has greatly enhanced our understanding and engineering of plasmonic nanostructures. Likewise, density functional approaches give much insight into molecular structure, electronic states, and vibrational modes. However, there is a clear and present need for further advancements in multiscale theoretical modeling that can combine sophisticated, realistic electronic structure, metallic dielectric response, and interactions with optical fields from the deep subwavelength toward macroscopic scales. Given the wealth of recent experimental progress and the prospects for computational advances, we expect that the melding of Raman spectroscopy, electronic transport techniques, and advanced theoretical treatments shall be a fruitful union for many years to come.

Acknowledgements

DN, YL and JBH acknowledge financial support from the Robert A. Welch Foundation award C-1636. DN and JBH further acknowledge LANCER, the Lockheed-Martin Advanced Nanotechnology Center of Excellence at Rice. The authors thank Daniel R. Ward for his prior work, construction of the Raman microscope system, and useful discussions; and M. W. Knight, N. J. Halas, P. Nordlander and J. M. Tour for their collaboration and useful discussions. We also acknowledge A. Garcia-Martin, J. C. Cuevas, L. Kronik and J. B. Neaton for their thoughtful insights.

References

1 E. Smith and G. Dent, *Modern Raman Spectroscopy: A Practical Approach*, Wiley, 2005.
2 A. Jorio, M. S. Dresselhaus, R. Saito and G. Dresselhaus, *Raman Spectroscopy in Graphene Related Systems*, Wiley, 2011.

3 T. P. Devereaux and R. Hackl, *Rev. Mod. Phys.*, 2007, **79**, 175–233.
4 M. Fleischmann, P. J. Hendra and A. J. McQuillan, *Chem. Phys. Lett.*, 1974, **26**, 163–166.
5 D. L. Jeanmaire and R. P. Van Duyne, *J. Electroanal. Chem. Interfacial Electrochem.*, 1977, **84**, 1–20.
6 M. G. Albrecht and J. A. Creighton, *J. Am. Chem. Soc.*, 1977, **99**, 5215–5217.
7 E. C. L. Ru and P. G. Etchegoin, *Principles of Surface-Enhanced Raman Spectroscopy: And Related Plasmonic Effects*, Elsevier Science Limited, 2009.
8 S. A. Maier, *Plasmonics: Fundamentals and Applications*, Springer, 2007.
9 L. Novotny and B. Hecht, *Principles of Nano-Optics*, Cambridge University Press, 2012.
10 M. J. Banholzer, J. E. Millstone, L. D. Qin and C. A. Mirkin, *Chem. Soc. Rev.*, 2008, **37**, 885–897.
11 J. Jiang, K. Bosnick, M. Maillard and L. Brus, *J. Phys. Chem. B*, 2003, **107**, 9964–9972.
12 E. Prodan, C. Radloff, N. J. Halas and P. Nordlander, *Science*, 2003, **302**, 419–422.
13 P. Nordlander, C. Oubre, E. Prodan, K. Li and M. I. Stockman, *Nano Lett.*, 2004, **4**, 899–903.
14 J. B. Lassiter, H. Sobhani, J. A. Fan, J. Kundu, F. Capasso, P. Nordlander and N. J. Halas, *Nano Lett.*, 2010, **10**, 3184–3189.
15 P. K. Jain, W. Huang and M. A. El-Sayed, *Nano Lett.*, 2007, **7**, 2080–2088.
16 A. L. Demming, F. Festy and D. Richards, *J. Chem. Phys.*, 2005, **122**, 184716–184717.
17 B. Pettinger, K. F. Domke, D. Zhang, G. Picardi and R. Schuster, *Surf. Sci.*, 2009, **603**, 1335–1341.
18 K. J. Savage, M. M. Hawkeye, R. Esteban, A. G. Borisov, J. Aizpurua and J. J. Baumberg, *Nature*, 2012, **491**, 574–577.
19 E. J. Blackie, E. C. L. Ru and P. G. Etchegoin, *J. Am. Chem. Soc.*, 2009, **131**, 14466–14472.
20 Z. Wang, S. Pan, T. D. Krauss, H. Du and L. J. Rothberg, *Proc. Natl. Acad. Sci. U. S. A.*, 2003, **100**, 8638–8643.
21 T. Dadosh, J. Sperling, G. W. Bryant, R. Breslow, T. Shegai, M. Dyshel, G. Haran and I. Bar-Joseph, *ACS Nano*, 2009, **3**, 1988–1994.
22 Z. Yang, J. Aizpurua and H. Xu, *J. Raman Spectrosc.*, 2009, **40**, 1343–1348.
23 Y. Uehara, Y. Kimura, S. Ushioda and K. Takeuchi, *Jpn. J. Appl. Phys.*, 1992, **31**, 2465.
24 A. Garcia-Martin, D. R. Ward, D. Natelson and J. C. Cuevas, *Phys. Rev. B: Condens. Matter Mater. Phys.*, 2011, **83**, 193404.
25 K. F. Domke, D. Zhang and B. Pettinger, *J. Phys. Chem. C*, 2007, **111**, 8611–8616.
26 C. C. Neacsu, J. Dreyer, N. Behr and M. B. Raschke, *Phys. Rev. B: Condens. Matter Mater. Phys.*, 2006, **73**, 193406.
27 J. Steidtner and B. Pettinger, *Phys. Rev. Lett.*, 2008, **100**, 236101.
28 W. Zhang, B. S. Yeo, T. Schmid and R. Zenobi, *J. Phys. Chem. C*, 2007, **111**, 1733–1738.
29 Z. Liu, S.-Y. Ding, Z.-B. Chen, X. Wang, J.-H. Tian, J. R. Anema, X.-S. Zhou, D.-Y. Wu, B.-W. Mao, X. Xu, B. Ren and Z.-Q. Tian, *Nat. Commun.*, 2011, **2**, 305.
30 N. Jiang, E. T. Foley, J. M. Klingsporn, M. D. Sonntag, N. A. Valley, J. A. Dieringer, T. Seideman, G. C. Schatz, M. C. Hersam and R. P. Van Duyne, *Nano Lett.*, 2011, **12**, 5061–5067.
31 E. C. Le Ru and P. G. Etchegoin, *Annu. Rev. Phys. Chem.*, 2012, **63**, 65–87.
32 K. Kneipp, Y. Wang, H. Kneipp, L. T. Perelman, I. Itzkan, R. Dasari and M. S. Feld, *Phys. Rev. Lett.*, 1997, **78**, 1667–1670.
33 S. M. Nie and S. R. Emery, *Science*, 1997, **275**, 1102–1106.
34 J. A. Dieringer, R. B. Lettan, K. A. Scheidt and R. P. Van Duyne, *J. Am. Chem. Soc.*, 2007, **129**, 16249–16256.
35 E. C. Le Ru, M. Meyer and P. G. Etchegoin, *J. Phys. Chem. B*, 2006, **110**, 1944–1948.
36 D. Zhang, Y. Xie, S. K. Deb, V. J. Davison and D. Ben-Amotz, *Anal. Chem.*, 2005, **77**, 3563–3569.
37 P. G. Etchegoin, E. C. Le Ru and M. Meyer, *J. Am. Chem. Soc.*, 2009, **131**, 2713–2716.
38 S. Berweger, J. M. Atkin, R. L. Olmon and M. B. Raschke, *J. Phys. Chem. Lett.*, 2012, **3**, 945–952.
39 N. Agraït, A. L. Yeyati and J. M. van Ruitenbeek, *Phys. Rep.*, 2003, **377**, 81–279.
40 B. Q. Xu and N. J. J. Tao, *Science*, 2003, **301**, 1221–1223.
41 L. Venkataraman, J. E. Klare, I. W. Tam, C. Nuckolls, M. S. Hybertsen and M. L. Steigerwald, *Nano Lett.*, 2006, **6**, 458–462.
42 A. M. Nowak and R. L. McCreery, *J. Am. Chem. Soc.*, 2004, **126**, 16621–16631.
43 R. L. McCreery, J. Wu and R. Prasad Kalakodimi, *Phys. Chem. Chem. Phys.*, 2006, **8**, 2572–2590.
44 Z. Ioffe, T. Shamai, A. Ophir, G. Noy, I. Yutsis, K. Kfir, O. Cheshnovsky and Y. Selzer, *Nat. Nanotechnol.*, 2008, **3**, 727–732.
45 J.-H. Tian, B. Liu, X. Li, Z.-L. Yang, B. Ren, S.-T. Wu, N. Tao and Z.-Q. Tian, *J. Am. Chem. Soc.*, 2006, **128**, 14748–14749.
46 T. Konishi, M. Kiguchi, M. Takase, F. Nagasawa, H. Nabika, K. Ikeda, K. Uosaki, K. Ueno, H. Misawa and K. Murakoshi, *J. Am. Chem. Soc.*, 2013, **135**, 1009–1014.
47 H. Park, A. K. L. Lim, A. P. Alivisatos, J. Park and P. L. McEuen, *Appl. Phys. Lett.*, 1999, **75**, 301–303.
48 W. Liang, M. P. Shores, M. Bockrath, J. R. Long and H. Park, *Nature*, 2002, **417**, 725–729.
49 E. A. Osorio, K. O'Neill, N. Stuhr-Hansen, O. F. Nielsen, T. Bjørnholm and H. S. J. van der Zant, *Adv. Mater.*, 2007, **19**, 281–285.
50 H. Park, J. Park, A. K. L. Lim, E. H. Anderson, A. P. Alivisatos and P. L. McEuen, *Nature*, 2000, **407**, 57–60.
51 J. Park, A. N. Pasupathy, J. I. Goldsmith, C. Chang, Y. Yaish, J. R. Petta, M. Rinkoski, J. P. Sethna, H. D. Abruna, P. L. McEuen and D. C. Ralph, *Nature*, 2002, **417**, 722–725.
52 A. N. Pasupathy, J. Park, C. Chang, A. V. Soldatov, S. Lebedkin, R. C. Bialczak, J. E. Grose, L. A. K. Donev,

J. P. Sethna, D. C. Ralph and P. L. McEuen, *Nano Lett.*, 2005, **5**, 203–207.
53 H. Song, Y. Kim, Y. H. Jang, H. Jeong, M. A. Reed and T. Lee, *Nature*, 2009, **462**, 1039–1043.
54 L. H. Yu and D. Natelson, *Nano Lett.*, 2004, **4**, 79–83.
55 H. Song, M. A. Reed and T. Lee, *Adv. Mater.*, 2011, **23**, 1583–1608.
56 D. R. Ward, N. K. Grady, C. S. Levin, N. J. Halas, Y. Wu, P. Nordlander and D. Natelson, *Nano Lett.*, 2007, **7**, 1396–1400.
57 J. M. Baik, S. J. Lee and M. Moskovits, *Nano Lett.*, 2009, **9**, 672–676.
58 A. Fursina, S. Lee, R. G. S. Sofin, I. V. Shvets and D. Natelson, *Appl. Phys. Lett.*, 2008, **92**, 113102.
59 J. B. Herzog, M. W. Knight, Y. Li, K. M. Evans, N. J. Halas and D. Natelson, 2012, submitted.
60 W. Zhu, M. G. Banaee, D. Wang, Y. Chu and K. B. Crozier, *Small*, 2011, **7**, 1761–1766.
61 D. R. Ward, N. J. Halas, J. W. Ciszek, J. M. Tour, Y. Wu, P. Nordlander and D. Natelson, *Nano Lett.*, 2008, **8**, 919–924.
62 D. Richards, R. G. Milner, F. Huang and F. Festy, *J. Raman Spectrosc.*, 2003, **34**, 663–667.
63 M. A. Ratner, *J. Phys. Chem.*, 1990, **94**, 4877–4883.
64 M. Galperin, M. A. Ratner and A. Nitzan, *J. Chem. Phys.*, 2004, **121**, 11965–11979.
65 B. C. Stipe, M. A. Rezaei and W. Ho, *Science*, 1998, **280**, 1732–1735.
66 S. Datta, *Electronic Transport in Mesoscopic Systems*, Cambridge University Press, 1997.
67 A. Zawadowski and M. Cardona, *Phys. Rev. B: Condens. Matter Mater. Phys.*, 1990, **42**, 10732–10734.
68 W. Akemann and A. Otto, *Philos. Mag. B*, 1994, **70**, 747–760.
69 A. Otto, *Phys. Status Solidi A*, 2001, **188**, 1455–1470.
70 A. Otto, W. Akemann and A. Pucci, *Isr. J. Chem.*, 2006, **46**, 307–315.
71 A. Otto and M. Futamata, in *Surface-Enhanced Raman Scattering: Physics and Applications*, ed. K. Kneipp, M. Moskovits and H. Kneipp, Springer-Verlag Berlin, Berlin, 2006, vol. 103, pp. 147–182.
72 D. R. Ward, D. A. Corley, J. M. Tour and D. Natelson, *Nat. Nanotechnol.*, 2011, **6**, 33–38.
73 L. Jensen, C. M. Aikens and G. C. Schatz, *Chem. Soc. Rev.*, 2008, **37**, 1061–1073.
74 J. R. Lombardi and R. L. Birke, *J. Phys. Chem. C*, 2008, **112**, 5605–5617.
75 A. T. Zayak, H. Choo, Y. S. Hu, D. J. Gargas, S. Cabrini, J. Bokor, P. J. Schuck and J. B. Neaton, *J. Phys. Chem. Lett.*, 2012, **3**, 1357–1362.
76 A. T. Zayak, Y. S. Hu, H. Choo, J. Bokor, S. Cabrini, P. J. Schuck and J. B. Neaton, *Phys. Rev. Lett.*, 2011, **106**, 083003.
77 D. Natelson, L. H. Yu, J. W. Ciszek, Z. K. Keane and J. M. Tour, *Chem. Phys.*, 2006, **324**, 267–275.
78 J. W. Park, A. N. Pasupathy, J. I. Goldsmith, A. V. Soldatov, C. Chang, Y. Yaish, J. P. Sethna, H. D. Abruna, D. C. Ralph and P. L. McEuen, *Thin Solid Films*, 2003, **438**, 457–461.
79 L. H. Yu, Z. K. Keane, J. W. Ciszek, L. Cheng, M. P. Stewart, J. M. Tour and D. Natelson, *Phys. Rev. Lett.*, 2004, **93**, 266802.
80 D. R. Ward, G. D. Scott, Z. K. Keane, N. J. Halas and D. Natelson, *J. Phys.: Condens. Matter*, 2008, **20**, 374118.
81 N. Liu, N. A. Pradhan and W. Ho, *J. Chem. Phys.*, 2004, **120**, 11371–11375.
82 G. V. Nazin, S. W. Wu and W. Ho, *Proc. Natl. Acad. Sci. U. S. A.*, 2005, **102**, 8832–8837.
83 X. H. Qiu, G. V. Nazin and W. Ho, *Phys. Rev. Lett.*, 2004, **92**, 206102.
84 M. Galperin and A. Nitzan, *J. Phys. Chem. Lett.*, 2011, **2**, 2110–2113.
85 M. Galperin and A. Nitzan, *Phys. Rev. B: Condens. Matter Mater. Phys.*, 2011, **84**, 195325.
86 D. K. Lambert, *Solid State Commun.*, 1984, **51**, 297–300.
87 D. M. Bishop, *J. Chem. Phys.*, 1993, **98**, 3179–3184.